

A novel GPU-based sonar simulator for real-time applications

Rômulo Cerqueira^{a,c}, Tiago Trocoli^a, Gustavo Neves^{a,c}, Sylvain Joyeux^a, Jan Albiez^{a,b}, Luciano Oliveira^c

^aBrazilian Institute of Robotics, SENAI CIMATEC, Salvador, Bahia, Brazil

^bRobotics Innovation Center, DFKI GmbH, Bremen, Germany

^cIntelligent Vision Research (IVISION) Lab, Federal University of Bahia, Salvador, Bahia, Brazil

Abstract

Mainly when applied in the underwater environment, sonar simulation requires great computational effort due to the complexity of acoustic physics. Simulation of sonar operation allows evaluating algorithms and control systems without going to the real underwater environment; that reduces the costs and risks of in-field experiments. This paper tackles with the problem of real-time underwater imaging sonar simulation by using the OpenGL shading language chain on GPU. Our proposed system is able to simulate two main types of acoustic devices: mechanical scanning imaging sonars and forward-looking sonars. The underwater scenario simulation is performed based on three frameworks: (i) OpenSceneGraph reproduces the ocean visual effects, (ii) Gazebo deals with physical forces, and (iii) the Robot Construction Kit controls the sonar in underwater environments. Our system exploits the rasterization pipeline in order to simulate the sonar devices, which are simulated by means of three parameters: the pulse distance, the echo intensity and the sonar field-of-view, being all calculated over observable objects shapes in the 3D rendered scene. Sonar-intrinsic operational parameters, speckle noise and object material properties are also considered as part of the acoustic image. Our evaluation demonstrated that the proposed system is able to operate close to or faster than the real-world devices. Also, our method generates visually realistic sonar images when compared with real-world sonar images of the same scenes.

Key words: Simulated sensor data, Sonar imaging, GPU-based processing, Robot Construction Kit (Rock), Underwater robotics.

1. Introduction

Simulation is an useful tool for designing and programming autonomous underwater vehicles (AUVs). That allows evaluating the vehicle behavior, without dealing with physical hardware or decision-making algorithms and control systems in real-time trials, as well as costly and time-consuming field experiments. AUVs usually demand expensive hardware and perform long-term data gathering operations, taking place in restrictive sites. When AUVs are not supported by an umbilical cable, and the underwater communication carries on by unreliable acoustic links, the vehicle should be able to make completely autonomous decisions, even with low-to-zero external assistance. While the analysis and interpretation of sensor data can be performed in a post-processing step, a real-time simulation is strongly necessary for testing and evaluation of vehicle's motion response, avoiding involved risks on real-world rides.

AUVs usually act below the photic zone, with high turbidity and huge light scattering. This makes the quality of image acquisition by optical devices limited by a short range, and artificially illuminated and clear visibility conditions. To tackle with that limitations, high-frequency sonars have been used primarily on AUVs' navigation and perception systems. Acoustic waves emitted by sonars are significantly less affected by water

attenuation, aiding operation at greater ranges even as low-to-zero visibility conditions, with a fast refresh rate. Although sonar devices usually solve the main shortcomings of optical sensors in underwater conditions, they provide noisy data of lower resolution and more difficult interpretation.

By considering sonar benefits and singularities along with the need to evaluate AUVs, recent works proposed ray tracing- [1, 2, 3, 4, 5, 6] and tube tracing-based [7] techniques to simulate acoustic data with very accurate results, although presenting a high computational cost. Bell [1] proposed a simulator based on optical ray tracing for underwater side-scan sonar imagery; images are generated by acoustic signals represented by rays, which are repeatedly processed, forming a 2D-array. Coiras and Groen [2] used frequency-domain signal processing to produce synthetic aperture sonar frames; in that method, the acoustic image is created by computing the Fourier transform of the acoustic pulse used to insonify the scene. For forward-looking sonar simulations, Saç *et al.* [3] described a sonar model by computing the ray tracing in frequency domain; when a ray hits an object in 3D space, three parameters are calculated to process the acoustic data: the Euclidean distance from the sonar axis, the intensity of returned signal by Lambert illumination model and the surface normal; the reverberation and shadow phenomena are also considered in the scene rendering. DeMarco *et al.* [4] used Gazebo and Robot Operating System (ROS) [8] integration to simulate acoustic sound pulses by ray tracing technique, also producing a 3D point cloud of the coverage area; the reflected intensity takes into account the object

Email addresses: romulo.cerqueira@ufba.br (Rômulo Cerqueira), tiago.trocoli@fieb.org.br (Tiago Trocoli), sylvain.joyeux@13robotics.com (Sylvain Joyeux), jan@ankerwin.de (Jan Albiez), lrebouca@ufba.br (Luciano Oliveira)

52 reflectivity, and the amount of Gaussian and salt-and-pepper
53 noises applied in the sonar image is empirically defined. Gu *et*
54 *al* [5] modeled a forward-looking sonar device, where the ultra-
55 sound beams are formed by a set of rays; the acoustic image is
56 significantly limited by a representation using only two colors:
57 white, when the ray strikes an object, and black for shadow areas.
58 Kwak *et al.* [6] improved the previous approach by adding
59 a sound pressure attenuation to produce the gray-scale sonar
60 frame, while the other physical characteristics related to sound
61 transmission are disregarded. Guériot and Sintès [7] introduce
62 a volume-based approach of energy interacting with the scene,
63 and collected by the receiving sonar; the sound propagation is
64 defined by series of acoustic tubes, being always orthogonal to
65 the current sonar view, where the reverberation and objects sur-
66 face irregularities are also addressed.

67 1.1. Contributions

68 This paper introduces a novel imaging sonar simulator that
69 presents some contributions when compared to the existing ap-
70 proaches. Instead of simulating the sound pulse paths and the
71 effects of their hits with the virtual objects, as presented by ray
72 tracing and tube tracing-based methods [1, 2, 3, 4, 5, 6, 7], we
73 take advantage of precomputed data (*e.g.*, normals, distances,
74 colors, angles) during the rasterization pipeline to compute the
75 acoustic frame. In addition, all raster data are handled on GPU,
76 accelerating then the simulation process with the guarantee of
77 real-time response, in contrast to the methods found in [1, 2, 3,
78 4]. Although the systems found in [1, 2, 3, 4, 5, 6, 7] focused
79 on the simulation of specific sonar device, our simulator is able
80 to reproduce two kinds of sonar devices: mechanical scanning
81 imaging sonar (MSIS) and forward-looking sonar (FLS). The
82 intensity measured back from the insonified objects depends
83 on surface normal directions and reflectivity, producing more
84 realistic simulated frames than binary representation, this lat-
85 ter found in [5, 6]. The speckle noise is modeled as a non-
86 uniform Gaussian distribution and applied to our final sonar
87 image, which approaches to real-world sonar operation, differ-
88 ently from [3, 4, 5, 6, 7]. On the other hand, we did not exploit
89 the additive noise as it was considered in [3, 4]. Finally, it is
90 noteworthy that our proposed system simulates physical phe-
91 nomena since they are constrained to real-time (*e.g.* decision-
92 making algorithms and control system tuning). Aware of this
93 real-time constraint, the high computational cost phenomena
94 such as reverberation is not included at this point, differently
95 from [3, 7].

96 The main goal here is to build quality and low time-con-
97 suming acoustic frames, according to underwater sonar image
98 formation and operation modes (see Section 2). The pulse dis-
99 tance, the echo intensity and the sonar field-of-view parameters
100 are extracted from the underwater scene during the rasteriza-
101 tion pipeline, and subsequently fused to generate the simulated
102 sonar data, as described in Section 3. Qualitative, quantitative
103 and time evaluation results for the two different sonar devices
104 are presented in Section 4, allowing the use of the proposed
105 simulator by real-time applications. Conclusions and future
106 work are drawn in Section 5.

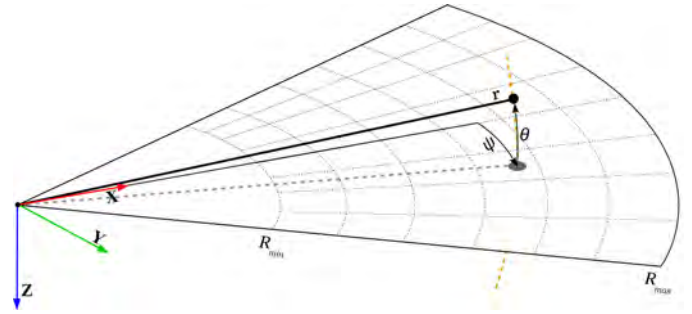


Figure 1: Imaging sonar geometry. By the projection process, all 3D points belonging to the same elevation arc (represented as dashed orange line) will be represented to the same image point in the 2D plane. Range r and azimuth angle ψ are measured, and elevation angle θ is lost. Sonar coverage area is defined by R_{min} and R_{max} .

107 2. Imaging sonar operation

108 Sonars are echo-ranging devices that use acoustic energy to
109 locate and survey objects in a desired area. The sonar trans-
110 ducer emits pulses of sound waves (or ping) until they hit any
111 object or are completely absorbed. When the acoustic signal
112 collides with a surface, part of this energy is reflected, while
113 other is refracted. The sonar data is built by plotting the echo
114 measured back versus time of acoustic signal. The transducer
115 reading in a given direction forms a *beam*. A single beam trans-
116 mitted from a sonar is illustrated in Fig. 1. The horizontal and
117 vertical beamwidths are represented by the azimuth ψ and ele-
118 vation θ angles, respectively, where each sampling along the
119 beam is named as *bin*. The sonar coverage area is defined by
120 R_{min} and R_{max} . Since the speed of sound underwater is known,
121 or can be measured, the time delay between the emitted pulses
122 and the respective echoes (named as *time of flight*) reveals how
123 far the objects are (distance r), as well as how fast they are mov-
124 ing. The backscattered acoustic power in each bin determines
125 the echo intensity value.

126 With different azimuth directions, the array of transducer
127 readings forms the final sonar image. Since all incoming sig-
128 nals converge to the same point, the reflected echoes could have
129 been originated anywhere along the corresponding elevation arc
130 at a fixed range, as depicted in Fig. 1. In the acoustic represen-
131 tation, the 3D information is lost in the projection into a 2D
132 image.

133 2.1. Sonar characteristics

134 Although sonar devices overcome main limitations of opti-
135 cal sensors, they present more difficult data interpretation due
136 to:

- 137 a) **Shadowing:** This effect is caused by objects blocking the
138 sound waves transmission, and causing regions behind them,
139 without acoustic feedback. These regions are defined by a
140 black spot in the sonar image, occluding part of the scene;
- 141 b) **Non-uniform resolution:** The amount of pixels used to
142 represent an echo intensity record in the Cartesian coordi-
143 nate system grows as its range increases. This situation
144 causes image distortions and object flatness;

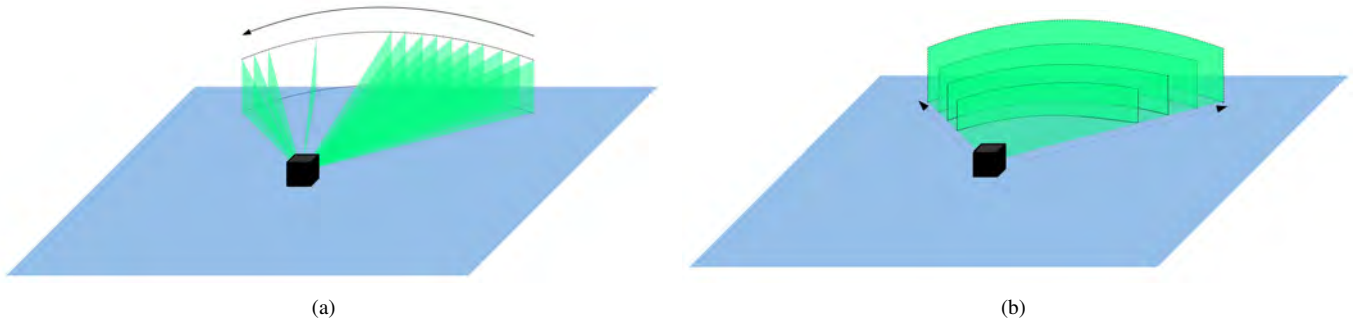


Figure 2: Different underwater sonar readings: (a) From a mechanical scanning imaging sonar and (b) from a forward-looking sonar.

- 145 c) **Changes in viewpoint:** Imaging the same scene from dif-
 146 ferent viewpoints can cause occlusions, shadows move-
 147 ments and significant changes of observable objects [9].
 148 For instance, when an outstanding object is insonified, its
 149 shadow is shorter, as the sonar becomes closer;
- 150 d) **Low signal-to-noise ratio (SNR):** Sonars suffer from low
 151 SNR mainly due the very-long-range scanning, and the
 152 presence of speckle noise introduced by acoustic wave in-
 153 terferences [10];
- 154 e) **Reverberation:** This phenomenon is caused when mul-
 155 tiple acoustic waves, returning from the same object, are
 156 detected over the same ping, producing duplicated objects.

157 2.2. Types of underwater sonar devices

158 The most common types of underwater acoustic sonars are
 159 MSIS and FLS. In the former, the sonar image is built for each
 160 pulse, with one beam per reading (see Fig. 2(a)); the resulting
 161 sonar images in MSIS are usually depicted on a display pulse by
 162 pulse, and the head position reader is rotated according to motor
 163 step angle. After a full 360° sector reading (or the desired sector
 164 defined by left and right limit angles), the accumulated sonar
 165 data is overwritten. The acquisition of a scanning image in-
 166 volves a relatively long time, introducing distortions caused by
 167 the vehicle movements. This sonar device is generally applied
 168 in obstacle avoidance [11] and navigation [12] applications. As
 169 illustrated in Fig. 2(b), the whole forward view of an FLS is
 170 scanned and the current data is overwritten by the next scan in a
 171 high frame rate, with all beams being read simultaneously; this
 172 is similar to a streaming video imagery for real-time applica-
 173 tions; this imaging sonar is commonly used for navigation [13],
 174 mosaicing [9], target tracking [14] and 3D reconstruction [15].

175 3. GPU-based sonar simulation

176 The goal of our work is to simulate two types of underwater
 177 sonar with low computational cost. The complete pipeline of
 178 the proposed simulator (from the virtual scene to the simulated
 179 acoustic data) is detailed in the following sections. The sonar
 180 simulator is written in C++ with OpenCV [16] support as Rock
 181 packages.

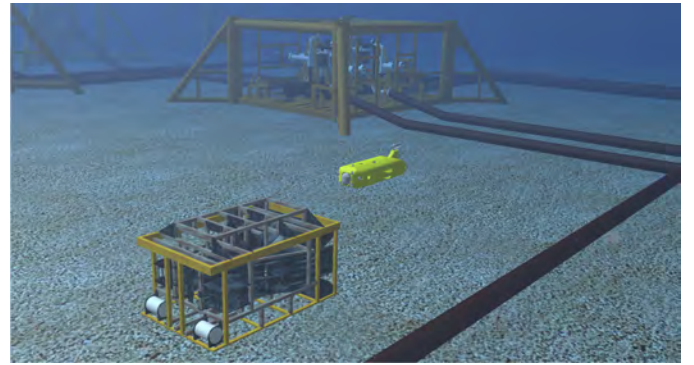


Figure 3: The virtual AUV in Rock-Gazebo underwater scene.

182 3.1. Rendering underwater scene

183 In Rock-Gazebo framework [17], Gazebo handles with phys-
 184 ical forces, while Rock’s visualization tools are responsible by
 185 the scene rendering. The graphical data in Rock are based
 186 on OpenSceneGraph framework, an open source C/C++ 3D
 187 graphics toolkit built on OpenGL. The osgOcean library is used
 188 to simulate the ocean visual effects. In our case, Rock-Gazebo
 189 integration provides the underwater scenario, allowing also real-
 190 time hardware-in-the-loop simulation with a virtual AUV.

191 All scene aspects, such as world model, robot parts (in-
 192 cluding sensors and joints) and other virtual objects are defined
 193 by simulation description files (SDF), which use the SDFor-
 194 mat [18], an XML format used to describe simulated models
 195 and environments for Gazebo. Visual and collision geome-
 196 tries of vehicle and sensors are also described in specific file
 197 formats. Each component described in the SDF file becomes
 198 a Rock component, which is based on the Orocos real-time
 199 toolkit (RTT) [19], providing I/O ports, properties and opera-
 200 tions as communication layers. When the models are loaded,
 201 Rock-Gazebo allows interaction between real world or simu-
 202 lated system components with the simulated models. A result-
 203 ing scene sample of this integration is illustrated in Fig. 3.

204 3.2. Sonar rendering

205 A rendering pipeline can be customized by defining GPU
 206 shaders. A shader is written in OpenGL Shading Language
 207 (GLSL) [20], a high-level language with a C-based syntax, which
 208 enables more direct control of graphics pipeline, avoiding the

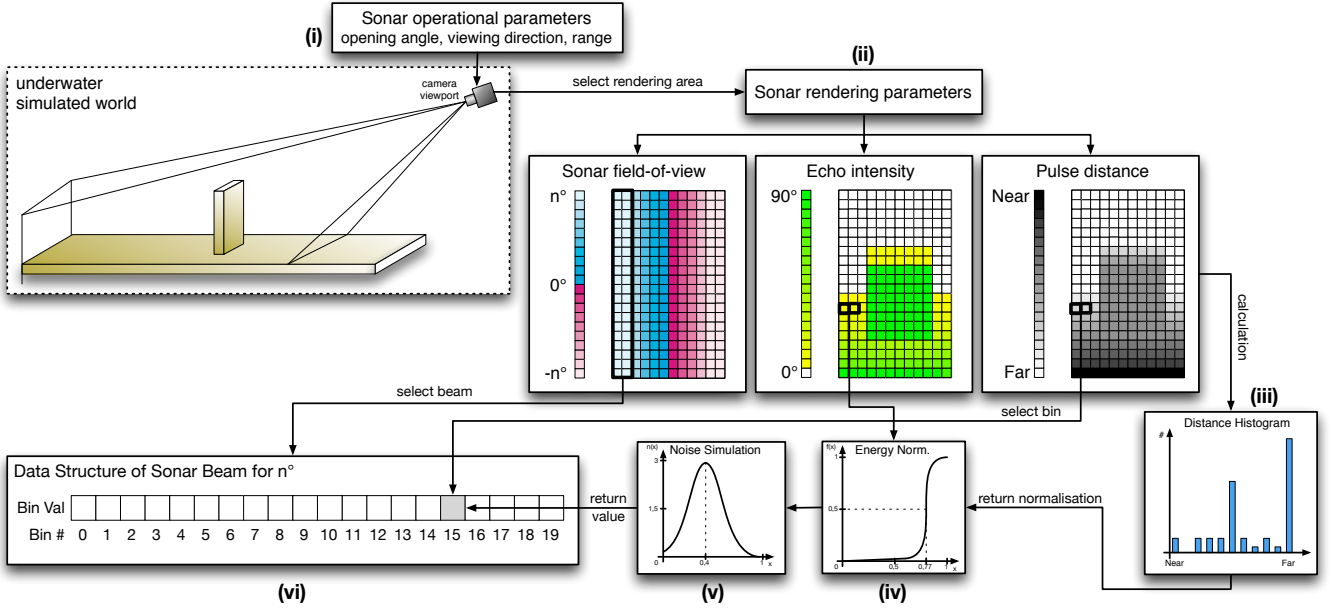


Figure 4: A graphical overview of the imaging sonar simulation process: (i) a virtual camera, specialized as the sonar device, samples the underwater scene; (ii) three 2D parameters are calculated by shader rendering on GPU: sonar field-of-view, echo intensity and pulse distance; the shader information is split into beam parts, according to the angle values, and the bin distance and echo intensity are defined by: (iii) distance histogram and (iv) energy normalization, respectively; (v) the speckle noise is applied to the final sonar data; (vi) and the simulated acoustic data is presented as Rock’s data type.

209 use of low-level or hardware-specific languages. Shaders can
 210 describe the characteristics of either a vertex or a fragment (a
 211 single pixel). Vertex shaders are responsible by transforming
 212 the vertex position into a screen position by the rasterizer, gener-
 213 ating texture coordinates for texturing, and lighting the vertex
 214 to determine each color. The rasterization results, in a set of
 215 pixels to be processed by fragment shaders, manipulate pixel
 216 location, depth and alpha values, and interpolated parameters
 217 from the previous stages, such as colors and textures.

218 In our work, the underwater scenes are sampled by a virtual
 219 camera (frame-by-frame), whose optical axis is aligned with the
 220 **opening angle**, the intended **viewing direction** and the cover-
 221 age **range** of the simulated sonar device (see Fig. 4(i)). To
 222 reproduce the sonar imaging operation by using virtual camera
 223 frames, three parameters are computed in fragment and vertex
 224 shaders, during the rendering pipeline. This way, we are able to
 225 use the precomputed geometric information during the image
 226 rasterization process on GPU. The three parameters to render
 227 the sonar device using a virtual camera are illustrated in Fig.
 228 4(ii), and are described as follows:

- 229 • **Pulse distance** simulates the time of flight of the acous-
 230 tic pulse, being calculated by the Euclidean distance be-
 231 tween the camera center and the object surface;
- 232 • **Echo intensity** represents the energy reflection of the
 233 sound wave, calculated from the object surface normal
 234 regarding the camera;
- 235 • **Sonar field-of-view** is represented by the camera field-
 236 of-view in the horizontal direction.

237 By default, the shader encodes the raster data in 8-bit color

238 channels for red, green, blue and alpha (RGBA). In our simu-
 239 lator, RGB channels are used to store the echo intensity, pulse
 240 distance and sonar field-of-view parameters to render the sonar
 241 from a virtual camera. The echo intensity parameter follows
 242 a real sonar common representation as 8-bit values. The pulse
 243 distance is replaced by the native GLSL 32-bit depth buffer to
 244 avoid precision limitation during the calculation of the distance
 245 histogram (see Fig. 4(iii)). As the field-of-view angle varies
 246 from the image center to both side directions, the sonar field-
 247 of-view is represented by 8-bit values without loss of precision.
 248 All of these three parameters are normalized into the interval
 249 $[0,1]$. For the echo intensity parameter, zero means no energy,
 250 while one means maximum echo energy. For pulse distance,
 251 the minimum value denotes a close object, while the maximum
 252 value represents a far one, limited by the sonar maximum range.
 253 Every sonar device has a maximum field-of-view; to represent
 254 this parameter in the rendering pipeline, the zero angle is in the
 255 center of the image, increasing until it reaches the half value of
 256 the maximum field-of-view of the simulated sonar device, for
 257 both sided borders; for example, if a sonar device has 120° of
 258 field-of-view, the zero angle is in the center of the virtual cam-
 259 era, spanning 60° to the left and 60° to the right.

260 In real-world sensing, surfaces usually present irregularities
 261 and different reflectance values. To render these surfaces
 262 in a virtual scene, the echo intensity values can also be defined
 263 by normal maps (see Fig. 5) and material property informa-
 264 tion (see Fig. 6). Normal mapping is a rendering technique,
 265 based on normal perturbation, that is used to simulate wrin-
 266 kles and dents on the object surface by using RGB textures on
 267 shaders. This approach consumes less computational resources
 268 for the same level of detail, compared with the displacement

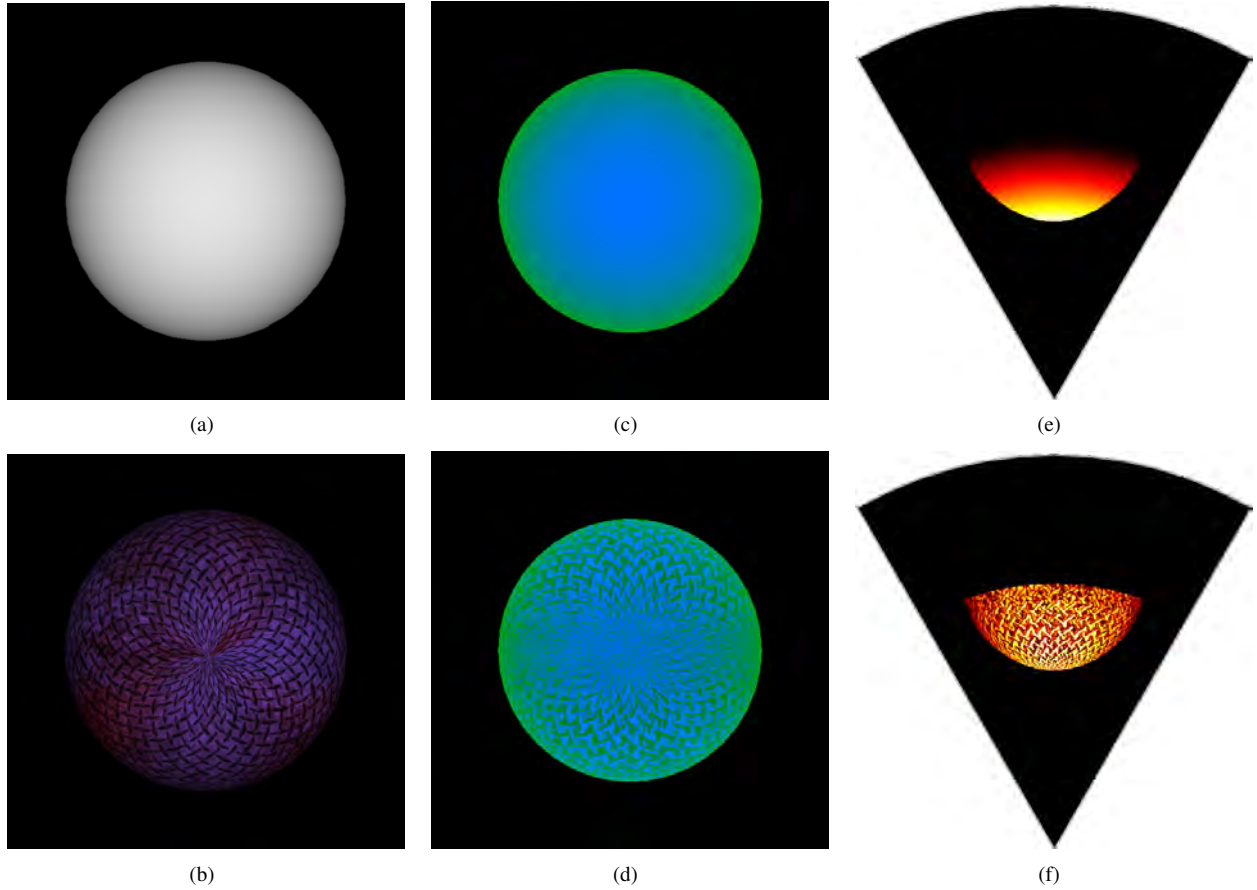


Figure 5: Example of shader rendering with normal mapping: A sphere without (a) and with texture (b); respective shader image representations of the spheres in (c) and (d), where the blue area represents the echo intensity parameter, while the green area means the pulse distance parameter. The final acoustic images are depicted in (e) and (f). By using normal mapping technique, the textures changes the normal directions, and the sonar image details the appearance of object surface, like in real world sensing.

269 mapping technique, because the geometry remains unchanged.
 270 Since normal maps are built in tangent space, interpolating the
 271 normal vertex and the texture, tangent, bi-tangent and normal
 272 (TBN) matrices are computed to convert the normal values into
 273 the world space. The visual differences of applying normal
 274 mapping in the actual scenes are illustrated in Figs. 5(a) and
 275 5(c); in the shader representation, in Figs. 5(e) and 5(b); and
 276 the final sonar image, in Figs. 5(d) and 5(f). The reflectance
 277 allows properly describing the intensity received back from ob-
 278 servable objects in shader processing, according to the material
 279 properties (for instance, aluminum has more reflectivity than
 280 wood and plastic). When an object has the reflectivity property
 281 defined, the reflectance value ρ is passed to the fragment shader
 282 and processed on GPU. So, the final pixel intensity represents
 283 the product of surface normal angle by the reflectance value ρ .
 284 The reflectance affects the shader representation, as depicted in
 285 Figs. 6(a), 6(b), 6(c) and 6(d)), with a final sonar image shown
 286 in Figs. 6(e), 6(f), 6(g) and 6(h).

287 3.3. Simulating operation of the sonar device

288 The sonar rendering parameters are used to compute the
 289 corresponding acoustic representation. Since the sonar field-
 290 of-view is radially spaced over the horizontal field-of-view of

291 the virtual camera (where all pixels in the same column have
 292 the same angle), the first step is to split the image into a num-
 293 ber of beams (beamed sub-images). Each column of the sonar
 294 field-of-view parameter is related with a respective beam vector,
 295 according to sonar bearings, as illustrated in Fig. 4(vi). In turn,
 296 one beam represents one or more columns. Each beamed sub-
 297 image is converted into bin intensities using the pulse distance
 298 and the echo intensity parameters. In a real imaging sonar, the
 299 echo measured back is sampled over time, and the bin number
 300 is proportional to the sensor range. In other words, the initial
 301 bins represent the closest distances, while the latest bins rep-
 302 resent the farthest ones. Therefore a distance histogram (see Fig.
 303 4(iii)) is computed in order to group the sub-image pixels with
 304 the respective bins, according to the pulse distance parameter
 305 and number of bins, and calculate the accumulated intensity in
 306 each bin.

307 Due to the acoustic beam spreading and absorption in the
 308 water, the final bins have less echo strength than the first ones.
 309 This is so, because the energy is twice lost in the environment.
 310 To tackle with that issue, sonar devices use an energy normal-
 311 ization based on time-varying gain for range dependence com-
 312 pensation, which spreads losses in the bins. In our simulation
 313 approach, the accumulated intensity, I_{bin} , in each bin (see Fig.

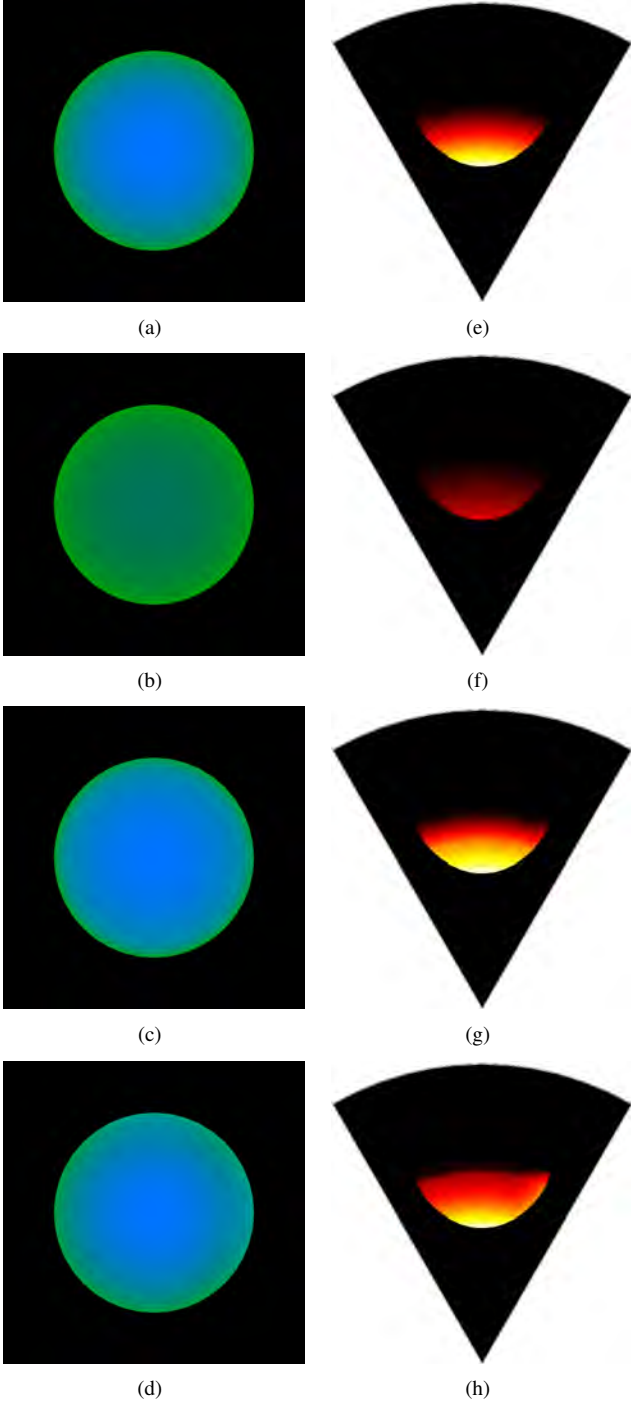


Figure 6: Examples of different reflectance values, ρ , applied in shader image representation of the same target, where blue is the echo intensity parameter and green is the pulse distance parameter: (a) raw image; (b) $\rho = 0.35$; (c) $\rho = 1.40$; and (d) $\rho = 2.12$. The following acoustic images are presented in (e), (f), (g) and (h).

314 4(iv)) is normalized as

$$315 \quad I_{bin} = \sum_{x=1}^N \frac{1}{N} \times S(i_x), \quad (1)$$

316 where x is the pixel location, N is the distance histogram value
317 (number of pixels) of that bin, $S(i_x)$ is a sigmoid function, i_x is

Table 1: Sonar device configurations used on experimental evaluation.

Device	# of beams	# of bins	Field of view	Down tilt	Motor Step
FLS	256	1000	120° x 20°	20°	-
MSIS	1	500	3° x 35°	0°	1.8°

318 the echo intensity value of the pixel x , and \times defines an element-
319 wise multiplication.

320 Finally, the sonar image resolution must be big enough to
321 contain all information of the bins. For that, the number of bins
322 involved is directly proportional to the sonar image resolution.

323 3.3.1. Noise model

324 Imaging sonar systems are disturbed by a multiplicative noise
325 known as speckle, which is caused by coherent processing of
326 backscattered signals from multiple distributed targets. This
327 effect degrades image quality and visual evaluation. Speckle
328 noise results in constructive and destructive interferences, which
329 are shown as bright and dark dots in the image. The noisy im-
330 age has been expressed, following [21]:

$$331 \quad y(t) = x(t) \times n(t), \quad (2)$$

332 where t is the time instant, $y(t)$ is the noised image, $x(t)$ is the
333 free-noise image, $n(t)$ is the speckle noise matrix, and \times defines
334 an element-wise multiplication.

335 This type of noise is well-modeled as a Gaussian distribu-
336 tion. The physical explanation is provided by the central limit
337 theorem, which states that the sum of many independent and
338 identically distributed random variables tends to behave as a
339 Gaussian random variable [22]. A Gaussian distribution is de-
340 fined by following a non-uniform distribution, skewed towards
341 low values, and applied as speckle noise in the simulated sonar
342 image (see Fig. 4(v)). This noise simulation is repeated for
343 each virtual acoustic frame.

344 3.3.2. Integrating sonar device with Rock

345 After the imaging sonar simulation process, from the virtual
346 underwater scene to the representation of the degraded acous-
347 tic sonar data by noise, the resulting sonar data is encapsulated
348 as Rock's sonar data type (see Fig. 4(vi)). This data type is
349 provided as I/O port of a Rock's component, allowing the inter-
350 action with other simulated models and applications.

351 4. Simulation results and experimental analysis

352 To evaluate our simulator, experiments were conducted by
353 using a 3D model of an AUV equipped with an MSIS and an
354 FLS. Different scenarios were casted and studied, considering
355 the sonar device configurations summarized in Table 1. In the
356 experimental analysis, as the scene frames are being captured
357 by the sonars, the resulting acoustic images are sequentially
358 presented, on-the-fly (see Figs. 7 and 8).

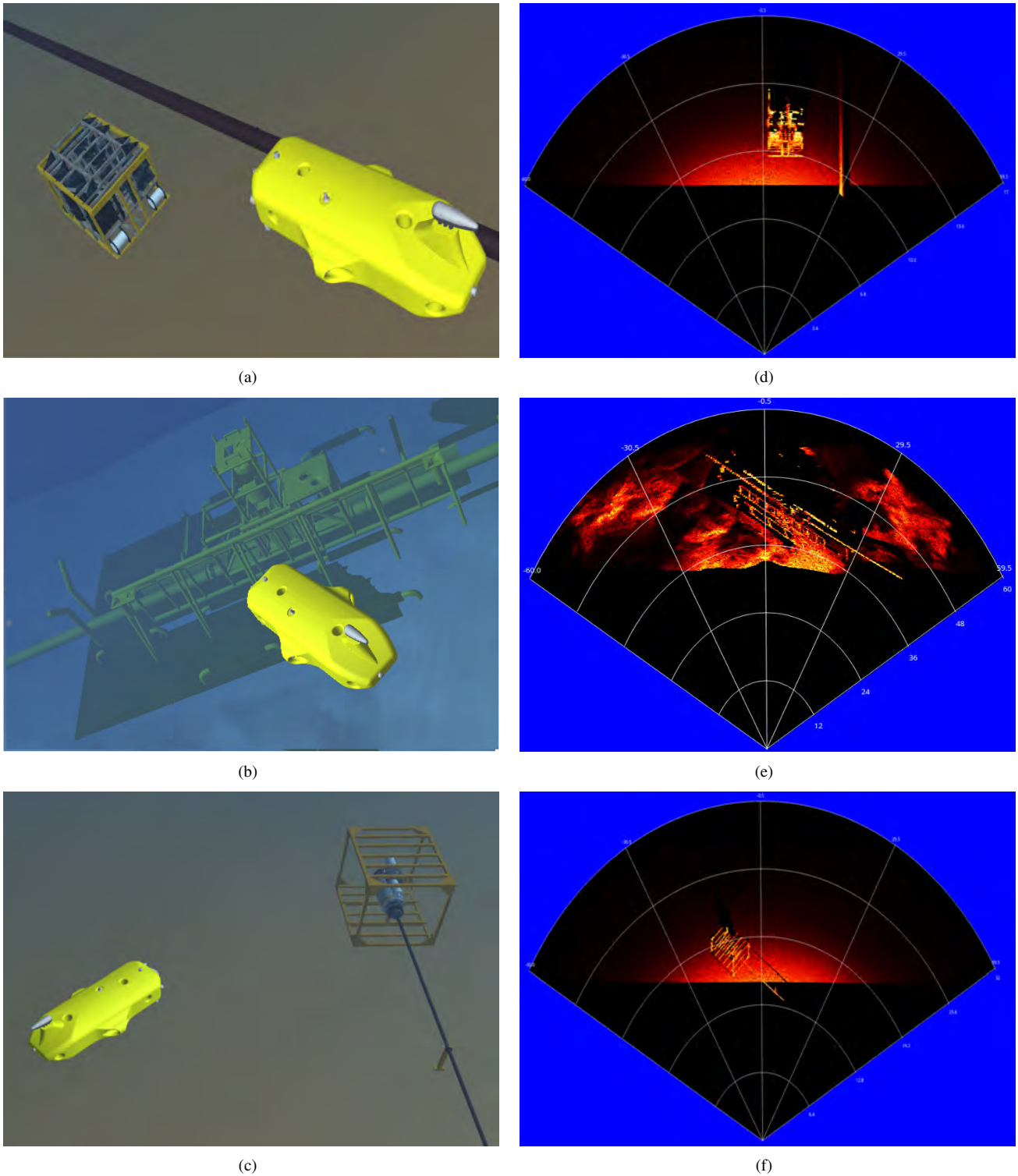


Figure 7: Forward-looking sonar simulation experiments: (a), (b) and (c) present the virtual underwater trials, while (d), (e) and (f) are the correspondent acoustic representations of each scenario, respectively.

359 *4.1. Experimental evaluation*

360 The virtual FLS from AUV was used to insonify the scenes
 361 from three distinct scenarios. A docking station, in parallel with
 362 a pipeline on the seabed, composes **the first scenario** (see Fig.
 363 7(a)); the target surface is well-defined in the simulated acous-

364 tic frame (see Fig. 7(d)), as well as the shadows and speckle
 365 noise; given that the docking station is metal-made, the tex-
 366 ture and reflectivity were set such that a higher intensity shape
 367 was resulted in comparison with the other observable targets.
 368 **The second scenario** presents the vehicle in front of a manifold

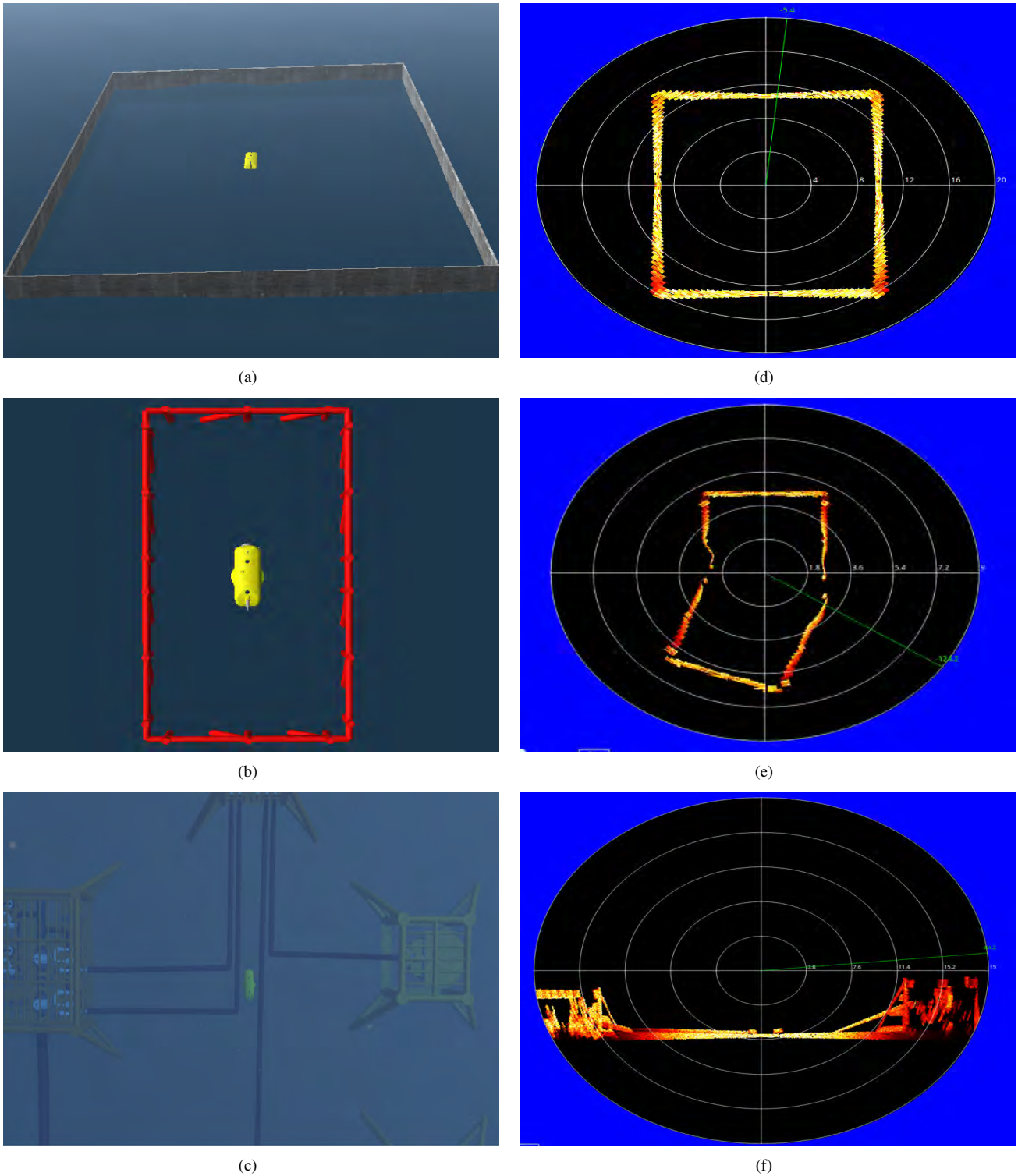


Figure 8: Experiments using mechanical scanning imaging sonar in three different scenarios (a), (b) and (c), and the respective processed simulated frames in horizontal orientation in (d) and (e), and vertical orientation in (f).

369 model in a non-uniform seabed (see Fig. 7(b)); the target model
 370 was insonified to generate the sonar frame from the underwa-
 371 ter scene (see Fig. 7(e)); the frontal face of the target, as well
 372 the portion of the seabed and the degraded data by noise, are
 373 clearly visible in the FLS image; also, a long acoustic shadow

374 is formed behind the manifold, occluding part of the scene. **The**
 375 **third scenario** contains a subsea isolation valve (SSIV) struc-
 376 ture, connected to a pipeline in the bottom (see Fig. 7(c)); the
 377 simulated acoustic image, depicted in Fig. 7(f), also present
 378 shadows, material properties and speckle noise effects. Due to

Table 2: Processing time to generate forward-looking sonar samples with different parameters.

# of samples	# of beams	# of bins	Field-of-view	Average time (ms)	Std dev (ms)	Frame rate (fps)
500	128	500	120° x 20°	54.7	3.7	18.3
500	128	1000	120° x 20°	72.3	8.9	13.8
500	256	500	120° x 20°	198.7	17.1	5.0
500	256	1000	120° x 20°	218.2	11.9	4.6
500	128	500	90° x 15°	77.4	11.8	12.9
500	128	1000	90° x 15°	94.6	10.2	10.6
500	256	500	90° x 15°	260.8	18.5	3.8
500	256	1000	90° x 15°	268.7	16.7	3.7

Table 3: Processing time to generate mechanical scanning imaging sonar samples with different parameters.

# of samples	# of bins	Field-of-view	Average time (ms)	Std dev (ms)	Frame rate (fps)
500	500	3° x 35°	8.8	0.7	113.4
500	1000	3° x 35°	34.5	1.6	29.0
500	500	2° x 20°	10.3	0.6	96.7
500	1000	2° x 20°	41.7	3.7	24.0

379 sensor configuration and robot position, the initial bins usually
 380 present a blind region in the three simulated scenes, caused by
 381 absence of objects at lower ranges, similar to real sonar images.
 382 It is noteworthy that the brightness of seafloor decreases as it
 383 is farther from sonar, because of the normal orientation of the
 384 surface.

385 The MSIS was also simulated in three different experiments.
 386 The robot in a big textured tank composes **the first scene** (see
 387 Fig. 8(a)); similar to the first scenario of FLS experiment, the
 388 reflectivity and texture were set to the target; the rotation of the
 389 sonar head position, by a complete 360° scanning, produced
 390 the acoustic frame of tank walls (see Fig. 8(d)). **The second**
 391 **scene** involves the vehicle’s movement during the data acqui-
 392 sition process; the scene contains a grid around the AUV (see
 393 Fig. 8(b)), captured by a front MSIS mounted horizontally; this
 394 trial induces a distortion in the final acoustic frame, because the
 395 relative sensor position with respect to the surrounding object
 396 changes, as the sonar image is being built (see Fig. 8(e)); in
 397 this case, the robot rotates 20° left during the scanning. **The**
 398 **last scene** presents the AUV over oil and gas structures on the
 399 sea bottom (see Fig. 8(c)); using an MSIS located in the back
 400 of the AUV with a vertical orientation, the scene was scanned
 401 to produce the acoustic visualization; as illustrated in Fig. 8(f),
 402 object surfaces present clear definition in the slice scanning of
 403 the sea-floor.

404 All the experimental scenarios was defined in order to pro-
 405 vide enough variability of specific phenomena usually found in
 406 real sonar images, such as acoustic shadows, noise interference,
 407 surface irregularities and properties, distortion during the acqui-
 408 sition process and changes of acoustic intensities. However, the
 409 speckle noise application is restricted to regions with acoustic
 410 intensity, as shown in Figs. 7(f) and 8(d). This fact is due to our
 411 sonar model be multiplicative (defined in Eq. 2). In real sonar

412 images, the noise also granulates the shadows and blind regions.
 413 The sonar simulator can be improved by inserting an additive
 414 noise to our model. The impact of incorporating additive noise
 415 on the image is more severe than that of multiplicative, and we
 416 decided to collect more data before including a specific addi-
 417 tive noise in our simulator, at this moment. A second feature
 418 missing in our simulated acoustic images are the ghost effects
 419 caused by reverberation. This lacking part can be addressed by
 420 implementation of a multi-path propagation model [23], where
 421 the signal propagates along several different paths, resulting in
 422 fading and reverberation effects. Simulating the multi-path re-
 423 flection is computationally costly, thus we need more time to
 424 model and include the reverberation phenomenon, considering
 425 the real-time constraints.

426 4.2. Computational time

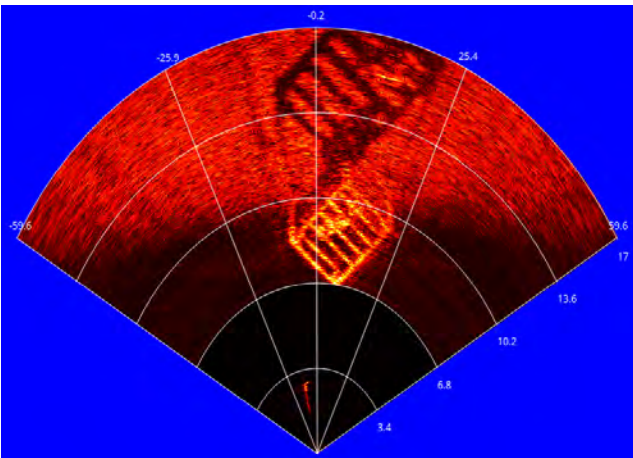
427 Performance evaluation of the simulator was assessed by
 428 considering the suitability to run real-time applications. The
 429 experiments were performed on a Intel Core i7 3540M proces-
 430 sor, running at 3 GHz with 16GB DDR3 RAM memory and
 431 NVIDIA NVS 5200M video card, with Ubuntu 16.04 64 bits
 432 operating system. The elapsed time of each sonar data is stored
 433 to compute the average time, standard deviation and frame rate
 434 metrics, after 500 iterations. The results found is summarized in
 435 Tables 2 and 3. After changing the sonar rendering parameters,
 436 such as number of bins, number of beams and field-of-view,
 437 the proposed approach generated the sonar samples with a high
 438 frame rate, for both sonar types, in comparison to real-world
 439 sonars. For instance, the Tritech Gemini 720i, a real forward-
 440 looking sonar sensor, with a field-of-view of 120° by 20° and
 441 256 beams, presents a maximum update rate of 15 frames per
 442 second; so, the obtained results allow the use of the sonar sim-
 443 ulator for real-time applications. Also, the MSIS produced data



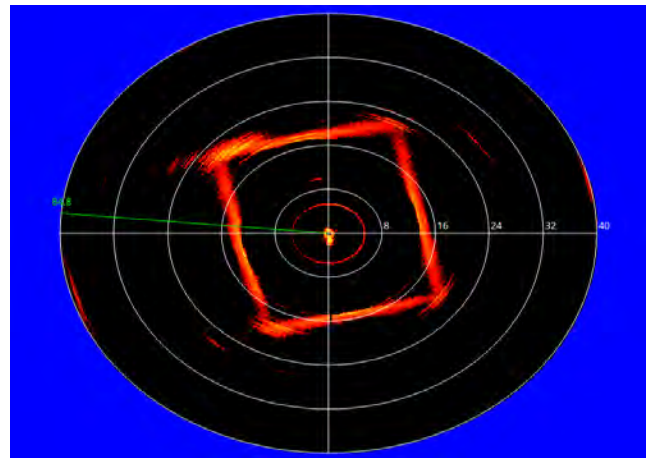
(a)



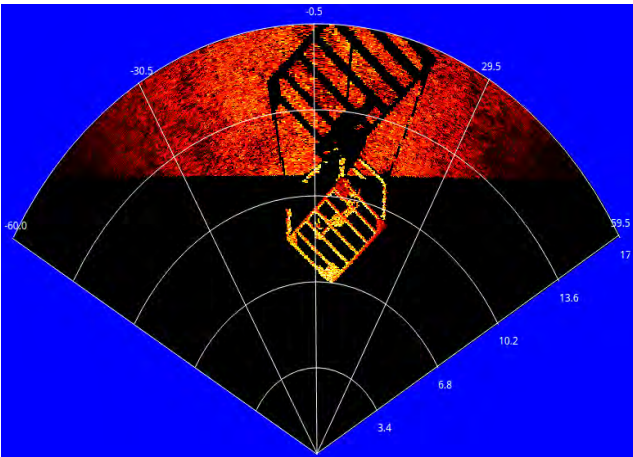
(b)



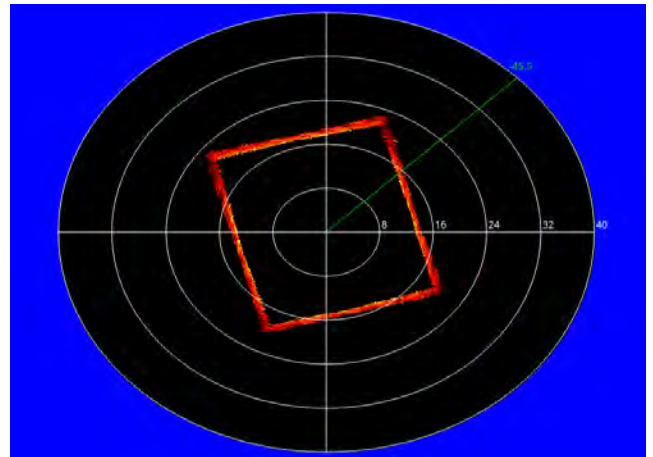
(c)



(d)



(e)



(f)

Figure 9: Target objects used in real and simulated experiments, insonified by Tritech Gemini 720i (FLS) and Tritech Micron DST (MSIS) sensors: (a) a subsea isolation valve (SSIV) and (b) a big tank. Real-world sonar and virtual images generated by our system: (c) sonar image of the SSIV captured with the FLS device and (e) the simulated image; (d) tank walls captured by the MSIS device and (f) the simulated representation.

444 in the simulator is able to complete a 360° scan sufficiently fast
 445 in comparison with a real sonar as Tritech Micron DST. For the
 446 FLS device, these rates are superior to the rates lists by De-
 447 Marco *et al* [4] (330ms) and Saç *et al* [3] (2.5min). For MSIS

448 type, to the best of our knowledge, there is no previous work
 449 for comparison.

450 According to previous results, since the number of bins is
 451 directly proportional to sonar image resolution, we can con-

clude that the number of bins used affects the computational time; when the number of bins increases, the simulator will have a bigger scene frame to compute and to generate the sonar data.

4.3. Quantitative evaluation of the simulated sonar image

Numerically assessing the performance of a sonar simulator is a non-trivial task. As sonar simulators are expected to work as trustworthy environment to avoid in-field experiments, the goal of quantitative evaluation should be to demonstrate that the real-world sonar image can be aligned with the synthetic one. Just two [3, 4] out of the seven works analyzed in Section 1 perform quantitative evaluation of the proposed simulators, although restricted only to computational time assessment.

Similarity should be carried out by considering a real-world and a virtual scene, both insonified by real and simulated sonar devices, respectively, at the same conditions. In other words, it means that we have to guarantee the same pose of the AUV in the real and virtual scenarios, which, in turn, should present the same elements being insonified; measuring the alignment of the images (real and simulated) works as comparing how much the simulated sonar image is similar to the real one with respect to pixel intensity and location, and image components.

The process of measuring the image quality can be performed by a set of metrics, among which, five were chosen to be used here: Mean-squared error (MSE), peak signal-to-noise ratio (PSNR), structural similarity index measure (SSIM), multi-scale structural similarity index measure (MS-SSIM), and scale invariant feature transform (SIFT). MSE calculates the cumulative square error between the reference and estimated images; values closer to zero are better. PSNR measures the peak error, expressed in terms of logarithmic scale; by handling with 8-bit grayscale images, the closer PSNR is to 99dB, the greater is similarity between the two images. SSIM evaluates the similarity of two images by performing a corresponding sliding window in the images; the more similar the images are, the average of window differences is closer to one. MS-SSIM is calculated as a weighted mean of SSIM rates, obtained for different scales of the reference and estimated images; as SSIM, the greater the values, the better is the results. SIFT compares the extracted interesting keypoints for both images; while the distance between the two set of descriptors over the keypoints in the two images approaches to zero, the greater the similarity degree. Here, all the metrics are normalized between zero and one range.

To evaluate the quality of the sonar images generated by our simulator, two real-world scenarios were modeled containing two target objects, which were insonified by an FLS and an MSIS: A SSIV (see Fig. 9(a)) submerged at Todos os Santos Bay, Salvador, Brazil; and the tank walls at DFKI Maritime Exploration Hall (see Fig. 9(b)). Figs. 9(c) and 9(e) are the results of the real and simulated sonar images of the SSIV, while Figs. 9(d) and 9(f) illustrate the real and simulated acoustic representations of the tank walls. The real sonar images were acquired using the FlatFish AUV [24]. After modeling the two scenarios, the five metrics were applied in order to compute the degree of similarity between each pair of sonar images. Table 4 summarizes the results.

Table 4: Similarity evaluation results between real-live and simulated sonar images.

Scene	MSE	PSNR	SSIM	MS-SSIM	SIFT
SSIV (Figs. 9(c), 9(e))	0.010	0.463	0.361	0.654	0.042
Tank (Figs. 9(d), 9(f))	0.004	0.489	0.834	0.895	0.288

Since the viewpoints in the real and the virtual scenes are approximated, the simulated images did not suffer from significant changes in the insonified objects, as explained in Section 2.1. However, the acoustic details and effects missing in the simulated images, such as reverberation and additive noise, probably influenced the results of PSNR, which did not even reach 50%, for the similarity of two scenes. SSIM and MS-SSIM take into account visual attributes of the images, such as luminance, contrast and structural terms, rather than pixel location; since the tank scene is an object simpler than the SSIV, in terms of insonified regions, and the FLS is more sensitive to the additive noise than MSIS, the results of the SSIM-based metrics presented higher similarity for MSIS images than FLS ones. SIFT has a limited performance when directly applied in images corrupted by multiplicative speckle noise [25]; this fact explains why the SIFT presented the worst similarity results for both sonar devices. MSE evaluates the two images in general, by considering the position of the elements in the scene; also, the two scenes were insonified by sonars presenting approximately the same poses, as well as, the simulator depicts the sonar image with echo intensity close to the real-world sonar image; these situations can explain why MSE was the metric with the best results, although a clear visual difference can still be observed in these latter two sonar images, due to the lack of the additive noise.

5. Conclusion and future work

A GPU-based simulator for imaging sonar was proposed here. The system is able to reproduce the operation mode of two different types of sonar devices (FLS and MSIS) in real-time. The real sonar image singularities, such as multiplicative noise, surface properties and acoustic shadows are addressed, and represented in the simulated acoustic images. The resulting acoustic representation of shadows are so accurate as the insonified objects. Considering the qualitative and quantitative results, the sonar simulator can be used by feature detection algorithms, based on corners, lines and shapes. Also, the computational time to build one sonar frame was calculated using different device settings. The vertex and fragment processing during the underwater scene rendering accelerates the simulated sonar image, providing an average time close to or better than real-world imaging devices. These results allow the use of

549 this imaging sonar simulator in real-time applications, such as
 550 obstacle detection and avoidance, and object tracking. We are
 551 working now on a way to add the reverberation effect to perform
 552 a more close-to-real sensing, without significantly affecting the
 553 computational time. We are also working on how to include an
 554 additive noise in the simulation of the acoustic images. We ex-
 555 pect that the addition of these two effects in the simulated sonar
 556 model will certainly improve the quantitative results, as well as,
 557 the visual perception of the resulting simulated images.

558 Acknowledgement

559 The presented work was done in cooperation with the Flat-
 560 Fish project, which is financed by Shell Brazil, the Brazilian
 561 Agency for Industrial Research and Innovation (EMBRAPPII)
 562 and the Brazilian National Agency of Petroleum, Natural Gas
 563 and Biofuels (ANP). The authors would like to thank all col-
 564 leagues at SENAI CIMATEC and DFKI for the support.

565 References

566 [1] Bell JM. Application of optical ray tracing techniques to the simulation
 567 of sonar images. *Optical Engineering* 1997;36(6):1806–13.
 568 [2] Coiras E, Groen J. Simulation and 3d reconstruction of side-looking sonar
 569 images. In: Silva S, editor. *Advances in Sonar Technology*; chap. 1. In-
 570 Tech; 2009, p. 1–15.
 571 [3] Saç H, Leblebicioğlu K, Bozdağı Akar G. 2d high-frequency
 572 forward-looking sonar simulator based on continuous surfaces ap-
 573 proach. *Turkish Journal of Electrical Engineering and Computer Sciences*
 574 2015;23(1):2289–303.
 575 [4] DeMarco K, West M, Howard A. A computationally-efficient 2d imag-
 576 ing sonar model for underwater robotics simulations in Gazebo. In:
 577 MTS/IEEE OCEANS Conference. 2015, p. 1–8.
 578 [5] Gu J, Joe H, Yu SC. Development of image sonar simulator for under-
 579 water object recognition. In: MTS/IEEE OCEANS Conference. 2013, p.
 580 1–6.
 581 [6] Kwak S, Ji Y, Yamashita A, Asama H. Development of acoustic camera-
 582 imaging simulator based on novel model. In: *IEEE International Con-
 583 ference on Environment and Electrical Engineering (EEEIC)*. 2015, p.
 584 1719–24.
 585 [7] Guériot D, Sintès C. Forward looking sonar data simulation through tube
 586 tracing. In: MTS/IEEE OCEANS Conference. 2010, p. 1–6.
 587 [8] Quigley M, Conley K, Gerkey BP, Faust J, Foote T, Leibs J, et al. ROS: an
 588 open-source robot operating system. In: *Workshop on Open Source Soft-
 589 ware, held at IEEE International Conference on Robotics and Automation
 590 (ICRA)*. 2009, p. 1–6.
 591 [9] Hurtós N. Forward-looking sonar mosaicing for underwater environments.
 592 Ph.D. thesis; Universitat de Girona; 2014.
 593 [10] Abbot J, Thurstone F. Acoustic speckle: theory and experimental analy-
 594 sis. *Ultrasonic Imaging* 1979;1(4):303–24.
 595 [11] Ganesan V, Chitre M, Brekke E. Robust underwater obstacle detection
 596 and collision avoidance. *Autonomous Robots* 2015;40(7):1–21.
 597 [12] Ribas D, Ridaó P, Neira J. *Underwater SLAM for structured environ-
 598 ments using an imaging sonar*. Springer-Verlag Berlin Heidelberg; 2010.
 599 [13] Fallon MF, Folkesson J, McClelland H, Leonard JJ. Relocating under-
 600 water features autonomously using sonar-based SLAM. *Journal of Ocean
 601 Engineering* 2013;38(3):500–13.
 602 [14] Liu L, Xu W, Bian H. A LBF-associated contour tracking method for
 603 underwater targets tracking. In: MTS/IEEE OCEANS Conference. 2016,
 604 p. 1–5.
 605 [15] Huang TA, Kaess M. Towards acoustic structure from motion for imaging
 606 sonar. In: *IEEE/RSJ International Conference on Intelligent Robots and
 607 Systems (IROS)*. 2015, p. 758–65.
 608 [16] Bradski G. The opencv library. *Doctor Dobbs Journal* 2000;25(11):120–
 609 6.

610 [17] Watanabe T, Neves G, Cerqueira R, Trocoli T, Reis M, Joyeux S, et al.
 611 The Rock-Gazebo integration and a real-time AUV simulation. In: *IEEE
 612 Latin American Robotics Symposium (LARS)*. 2015, p. 132–8.
 613 [18] SDF. <http://sdformat.org/>; 2017. Accessed: 2017-04-23.
 614 [19] Soetens P, Bruyninckx H. Realtime hybrid task-based control for robots
 615 and machine tools. In: *IEEE International Conference on Robotics and
 616 Automation (ICRA)*. 2005, p. 260–5.
 617 [20] Rost RJ, Licea-Kane B, Ginsburg D, Kessenich JM, Lichtenbelt B, Malan
 618 H, et al. *OpenGL shading language*. 3rd ed.; Addison-Wesley Profes-
 619 sional; 2009.
 620 [21] Lee J. Digital image enhancement and noise filtering by use of local
 621 statistics. *IEEE Transactions on Pattern Analysis and Machine Intelli-
 622 gence* 1980;2(2):165–8.
 623 [22] Papoulis A, Pillai S. *Probability, random variables and stochastic pro-
 624 cesses*. McGraw Hill; 2002.
 625 [23] Huang J. Simulation and modeling of underwater acoustic communica-
 626 tion channels with wide band attenuation and ambient noise. Ph.D. thesis;
 627 Carleton University; 2015.
 628 [24] Albiez J, Joyeux S, Gaudig C, Hilljegerdes J, Kroffke S, Schoo C, et al.
 629 FlatFish - a compact AUV for subsea resident inspection tasks. In:
 630 MTS/IEEE OCEANS Conference. 2015, p. 1–8.
 631 [25] Suganya G, Vasanthi D. An improvement of image registration based
 632 on sift algorithm along with non linear diffusion. *Internation Journal of
 633 Modern Trends in Engineering and Science* 2016;3(4):70–3.